

Spectral Mapping of the Intermediate Polar DQ Herculis

R. K. Saito

Departamento de Astronomía y Astrofísica, Pontificia Universidad Católica de Chile,
Vicuña Mackenna 4860, Casilla 306, Santiago 22, Chile

rsaito@astro.puc.cl

R. Baptista

Departamento de Física, Universidade Federal de Santa Catarina, Trindade, 88040-900,
Florianópolis, SC, Brazil

K. Horne

School of Physics and Astronomy, University of St. Andrews, KY16 9SS, Scotland, UK

and

P. Martell

University of Wisconsin Center – Marinette, 750 W. Bay Shore Street, Marinette, WI
54143, USA

Received _____; accepted _____

ABSTRACT

We report an eclipse mapping study of the intermediate polar DQ Her based on time-resolved optical spectroscopy ($\Delta\lambda \sim 3800 - 5000 \text{ \AA}$) covering 4 eclipses. The spectra were sliced into 295 narrow passbands in the continuum and in the lines, and the corresponding light curves were analysed to solve for a set of monochromatic maps of the disk brightness distribution and for the flux of an additional uneclipsed component in each band. Eclipse maps of the He II $\lambda 4686$ line indicate that an azimuthally- and vertically-extended bright spot at disk rim is important source of reprocessing of x-rays from the magnetic poles. The disk spectrum is flat with no Balmer or Helium lines in the inner regions, and shows double-peaked emission lines in the intermediate and outer disk regions while the slope of the continuum becomes progressively redder with increasing radius. The inferred disk temperatures are in the range $T \simeq 13500 - 5000 \text{ K}$ and can be reasonably well described by a steady-state disk with mass accretion rate of $\dot{M} = (2.7 \pm 1.0) \times 10^{-9} M_{\odot} \text{ yr}^{-1}$. A comparison of the radial intensity distribution for the Balmer lines reveals a linear correlation between the slope of the distribution and the transition energy. The spectrum of the uneclipsed light is dominated by Balmer and He I lines in emission (probably from the extended nova shell) with narrow absorption cores (likely from a collimated and optically thick wind from the accretion disk). The observed narrow and redshifted Ca II $\lambda 3934$ absorption line in the total light spectra plus the inverse P-Cygni profiles of the Balmer and He II $\lambda 4686$ emission lines in spectra of the asymmetric component indicate radial inflow of gas in the innermost disk regions and are best explained in terms of magnetically-controlled accretion inside the white dwarf magnetosphere. We infer projected radial inflow velocities of $\sim 200 - 500 \text{ km s}^{-1}$, significantly lower than both the rotational and the free-fall velocities for the corresponding

range of radii. A combined net emission He II plus $H\beta$ low-velocity eclipse map reveals a twisted dipole emitting pattern near disk center. This is interpreted as being the projection of accretion curtains onto the orbital plane at two specific spin phases, as a consequence of the selection in velocity provided by the spectral eclipse mapping.

Subject headings: accretion, accretion disks – binaries: eclipsing – novae, cataclysmic variables – stars: individual (DQ Her)

1. Introduction

In many cataclysmic variable stars, the magnetic field of the white dwarf (primary star) is sufficiently weak to be neglected. On the other hand, in systems like the AM Her stars, the magnetic field dominates completely the accretion flow (Hellier 2001). Intermediate cases can lead to a complex range of phenomena. This occurs in the intermediate polar stars, where a magnetic field of moderate strength ($B \lesssim 10^7 G$) allows the combination of characteristics of non-magnetic systems (in the outer disk regions) with characteristics of highly magnetic systems (in the regions close to the white dwarf).

In intermediate polars the inner regions of the accretion disk are disrupted by the magnetic field of the white dwarf and the infalling plasma is forced to follow the field lines down to the star’s surface at one or both the magnetic poles, transforming kinetic energy into radiation. Part of this energy can be reprocessed in other sites of the binary, leading to pulsations at the white dwarf rotation period and/or its beating with the orbital period (Warner 1986).

DQ Her, or Nova Her 1934, is a deeply eclipsing cataclysmic variable (orbital period $P = 4.6 h$) and the prototype of the subclass of intermediate polars, showing a coherent 71 s pulsation (Walker 1956). Due to the high inclination of the system ($i = 86.5^\circ$; Horne et al. 1993) the white dwarf, accretion disk and bright spot are occulted by the secondary star, allowing the emission from these different light sources to be separated and spatially resolved by indirect imaging techniques such as eclipse-mapping (Horne 1985) and Doppler tomography (Marsh & Horne 1988).

Here we report the results of an eclipse-mapping study of the spectra and structure of the accretion disk of DQ Her based on time-resolved spectroscopy of 4 eclipses collected on July 1987. The observations are described in Section 2. Data analysis procedures are given in Section 3. In Section 4 we investigate the disk spatial structure in the emission lines and

in the continuum and we present spatially resolved spectra of the disk, gas stream and of the uneclipsed light. The results are discussed in Section 5 and summarized in Section 6. In the Appendix A we discuss the ability to reconstruct the full-width-half-maximum distribution of emission lines with spectral mapping techniques.

2. Observations

The data consist of 3272 spectra obtained with the Double Spectrograph at the Hale 5 m telescope, using the 2D-FRUTTI detector on the nights of 1987 July 3 – 4. The runs cover the eclipse cycles 62105, 62106, 62110 and 62111, according to ephemeris of Africano & Olson (1981). The integration time for each spectrum was 10 s, and the usable spectral coverage is $\Delta\lambda \sim 3800 - 5000 \text{ \AA}$. The reader is referred to Martell et al. (1995) for a detailed description of the observations and of the data reduction procedures.

The data were corrected to the rest frame of the white dwarf by removing its orbital velocity $K_1 = 140 \text{ km s}^{-1}$ (Horne et al. 1993) from the spectra, and then binned to a resolution of 130 km s^{-1} per bin (2 \AA pixel^{-1} at 4500 \AA). In the present work we analyse only the data around eclipse, in the phase range -0.1 to $+0.1$, comprising a subset of 1073 spectra from the original data set.

Fig. 1 shows average spectra prior to (phase range -0.09 to -0.08 cycle), after ($+0.10$ to $+0.11$) and at mid-eclipse (-0.02 to $+0.02$). The spectra show Balmer emission lines, a strong He II 4686 line, weak He I and He II lines and a few metal absorption lines on top of a flat continuum. The emission lines show a clear double-peaked profile at mid-eclipse. The Balmer lines are more prominent at mid-eclipse than outside eclipse, indicating that their emission is less concentrated towards disk center than that of the continuum.

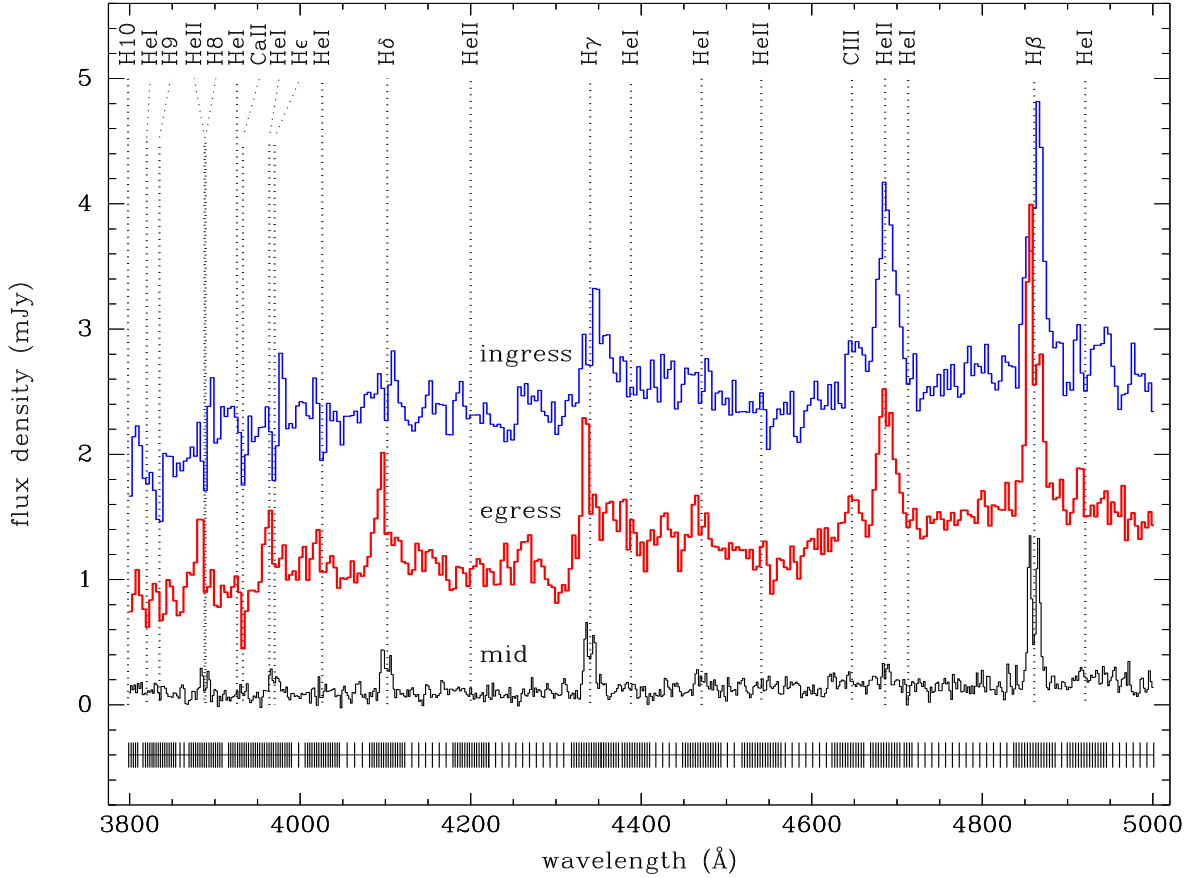


Fig. 1.— Average ingress (dark grey, phase range -0.09 to -0.08 cycle), egress (light grey, $+0.10$ to $+0.11$ cycle) and mid-eclipse (black, -0.02 to $+0.02$ cycle) spectra of DQ Her, from the combined eclipse cycles 62105, 62106, 62110 and 62111 (see text). Vertical dotted lines indicate the emission/absorption lines. Horizontal ticks mark the 295 passbands used to extract light curves. For a better visualization the ingress and egress spectra are vertically displaced by -1.4 and 1.7 mJy , respectively.

3. Data analysis

3.1. Light-curve construction

The spectra were divided into 295 narrow passbands; 72 continuum passbands, typically 8 Å wide, and 223 velocity-resolved bands of 200 $km\ s^{-1}$ for the 22 lines marked in Fig. 1. In defining the velocity-resolved line bins, we neglected the small systemic velocity of the object ($\gamma = 5 \pm 5\ km\ s^{-1}$, Horne et al. 1993). For the passbands including emission lines, the light curve comprises the total flux at the corresponding bin, with no subtraction of a possible continuum contribution.

Light curves were extracted for each band, combining the average flux of the four data sets on the corresponding wavelength range in phase bins of 0.0025 cycles. The error bars are taken as the standard deviation with respect to the average flux at each phase bin. The resulting light curves were phase-folded according to the ephemeris of Africano & Olson (1981).

$$T_{\text{mid}} = \text{HJD } 2434954.943899(2) + 0.193620897(5)\ \text{E}. \quad (1)$$

We remark that, because the 71 s oscillation was not removed from the light curves, the resulting eclipse maps contain the combined light distribution of the steady, unpulsed light and a time averaged distribution of the pulsed light. Nevertheless, since the 71 s accounts for, at most, 2 – 3 % of the total flux (Martell et al. 1995), the influence of the pulsed light on the overall disk brightness distribution is small. Light curves and eclipse maps for the H β and HeII 4686 lines are shown in Figs. 2 and 3, respectively. Contour curves in these figures enclose the regions of the eclipse maps at and above the 15 σ level of statistical significance.

3.2. Eclipse-mapping

We used maximum-entropy eclipse-mapping techniques (Horne 1985; Baptista & Steiner 1993) to solve for a map of the disk brightness distribution and for the flux of an additional uneclipsed component in each spectral band. The reader is referred to Baptista (2001) for a review on the eclipse-mapping method.

As our eclipse map we adopted a flat grid of 65×65 pixels centered on the primary star with side $2 R_{L_1}$, where R_{L_1} is the distance from the disk center to the inner Lagrangian point (L_1). In this work we adopted a Roche lobe size of $R_{L_1} = 0.766 R_\odot$ (Petterson 1980). The eclipse geometry is defined by the mass ratio q , which sets the shape and the relative size of the Roche lobes, and the inclination i , which determines the shape and extension of the shadow of the secondary star projected onto the orbital plane. We adopted the values by Horne et al. (1993), $q = 0.66 \pm 0.04$ and $i = 86.5^\circ \pm 1.6^\circ$. This combination of parameters ensures that the white dwarf is at the center of the map.

Before applying eclipse mapping techniques to a high inclination system such as DQ Her, it is important to address the question whether the disk rim can hide parts of the accretion disk from view (thereby leading to unreliable results). In particular, a vertically-extended, thick disk rim could lead to an important self-occultation effect on the disk side closest to the observer if the disk half-opening angle is $\beta \gtrsim (90^\circ - i)$. An estimate of the disk half-opening angle in DQ Her comes from the recent work of Saito & Baptista (2009). They applied eclipse mapping techniques to trace the changes in surface brightness distribution along the 71 s pulsation cycle and found that a vertically-extended bright spot at disk rim is the main site of emission of the 71 s optical oscillations. The upper side of the bright spot is illuminated by one of the magnetic poles once per cycle, while the lower side of the bright spot is illuminated by the other pole roughly half a cycle later. From the difference in the projected position of the upper and lower bright spot sides in their eclipse maps,

they inferred a vertical thickness of $H = (7.4 \pm 0.4) \times 10^{-3} R_{\odot} [\tan(i)/16.35]^{-1}$ ¹, where the term within brackets is unity for $i = 86.5^{\circ}$. Combined with a bright spot radial distance of $R_{BS} = (0.44 \pm 0.02) R_{\odot}$ (see Section 4.1), this leads to $\beta = \arctan(H/2R_{BS}) = 0.5^{\circ} - 0.002^{\circ}$ for $i = 86.5^{\circ} - 89^{\circ}$. The lowest range of values for β is hard to be interpreted by the steady-state disks model, where flared disks are expected, with the vertical tickness H proportional to the mass accretion rate \dot{M} and increasing with radius with by factor $H \propto r^{9/8}$. The inferred value of β decreases with increasing inclination, and the inequality $\beta < (90^{\circ} - i)$ holds for any reasonable inclination ($i > 70^{\circ}$). Hence, self-obscuration by the disk rim is not an issue in DQ Her. The fact that the bright illumination pattern that rotates with the 71 s pulsation period in the inner disk regions remains visible when it is passing in the disk side near the observer (Saito & Baptista 2009) yields additional support for the above statement. We are therefore confident that no distortion effects caused by self-obscuration by the disk rim arise when applying eclipse mapping techniques to the DQ Her light curves.

For the reconstructions we used the default of limited azimuthal smearing of Rutten et al. (1992), which is better suited for recovering asymmetric structures than the original default of full azimuthal smearing (c.f., Baptista et al. 1996). Simulations showing the ability of the eclipse mapping method to reconstruct asymmetric brightness distributions (even under unfavorable conditions of low S/N and incomplete phase coverage) are presented and discussed by Baptista (2001) and Baptista & Catalán (2001). We used a radial blur width $\Delta r = 0.0185R_{L1}$ and an azimuthal blur width $\Delta\theta = 20^{\circ}$.

The statistical uncertainties in the eclipse maps were estimated with a Monte Carlo procedure (e.g., Rutten et al. 1992). For each narrow band light curve, a set of 20 artificial

¹In Saito & Baptista (2009) this value is mistakenly quoted as the bright spot vertical half-thickness.

light curves was generated in which the data points were independently and randomly varied according to a Gaussian distribution with standard deviation equal to the uncertainty at that point. The light curves were fitted with the eclipse-mapping code to produce a set of randomized eclipse maps. These were combined to produce an average map and a map of the residuals with respect to the average, which yields the statistical uncertainty at each pixel. The uncertainties obtained with this procedure were used to estimate the errors in the derived radial intensity and temperature distributions as well as in the spatially resolved spectra. We also divided each eclipse map by the map of the residuals with respect to the average to produce maps of the inverse of the relative errors, or signal-to-noise ratio maps (Baptista & Bortoletto 2004). The S/N maps are overplotted on the corresponding eclipse maps in Figs. 2 and 3 as a contour line for $S/N = 15$. All structures in the eclipse maps are significant at a confidence level equal to or above 15σ .

4. Results

4.1. Disk structures

Fig. 2 shows eclipse maps of H β for a set of 5 velocity bins. Similarly, Fig. 3 shows velocity-resolved eclipse maps for the He II 4686 line. The velocity-resolved H β (and, to a less extent, the He II 4686 line) light curves show the expected behavior for the eclipse of gas rotating in the prograde sense (rotational disturbance), with the blue side being eclipsed earlier than the red side. The eclipse maps in symmetric velocity bins do not show the reflection symmetry around the line joining both stars expected for the emission from a symmetric disk around the white dwarf.

The clear egress shoulder in the light curves reveals an azimuthally-extended asymmetry in the outer parts of the disk extending $\simeq 90^\circ$ ahead of the intersection of the stream

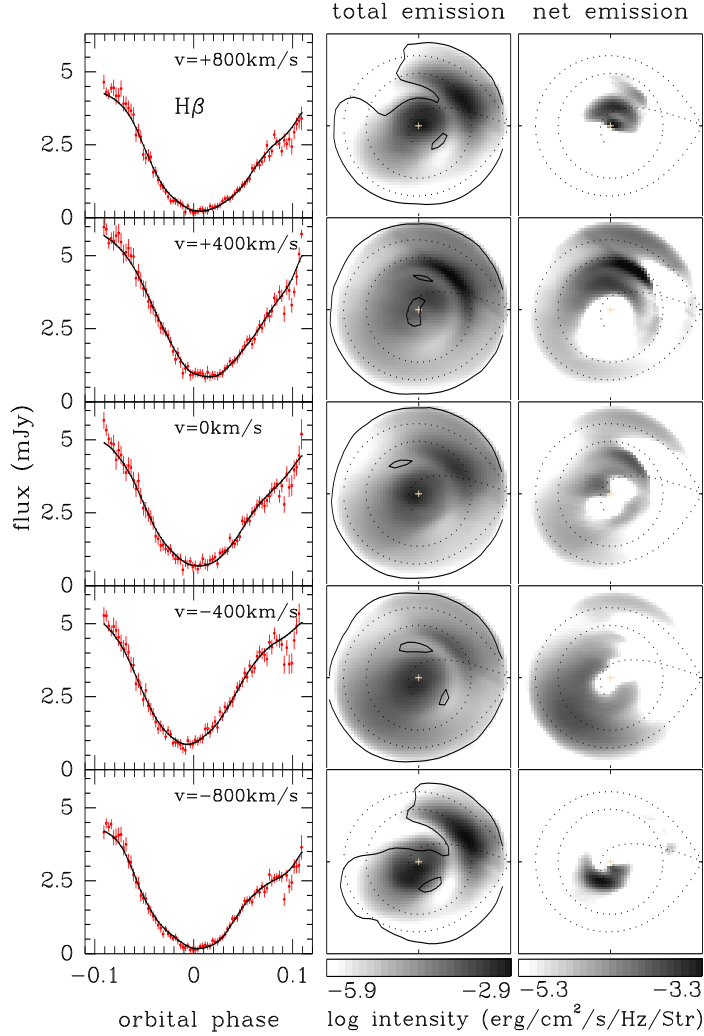


Fig. 2.— Data and model light curves and eclipse maps for $H\beta$ ($\lambda 4861$) at five velocity bins ($v = \pm 800, \pm 400, 0 \text{ km s}^{-1}$, $\Delta v = 200 \text{ km s}^{-1}$). The left panels show the data (dots with error bars) and model (solid lines) light curves. The middle panels show the corresponding eclipse maps for the total emission (line + continuum) in a logarithmic greyscale. Brighter regions are indicated in black; fainter regions in white. A cross marks the center of the disk; dotted lines show the Roche lobe, the gas stream trajectory and a circle of radius $R_{BS} = 0.57 R_{L1}$ corresponding to the bright spot position; the secondary is to the right of each map and the stars rotate counter-clockwise. Contour curves enclose the regions at and above the 15σ level of statistical significance. The right panels show eclipse maps of the net line emission in each case; the notation is similar to that of the middle panels. The horizontal bars indicate the logarithmic intensity level of the greyscale in each column.

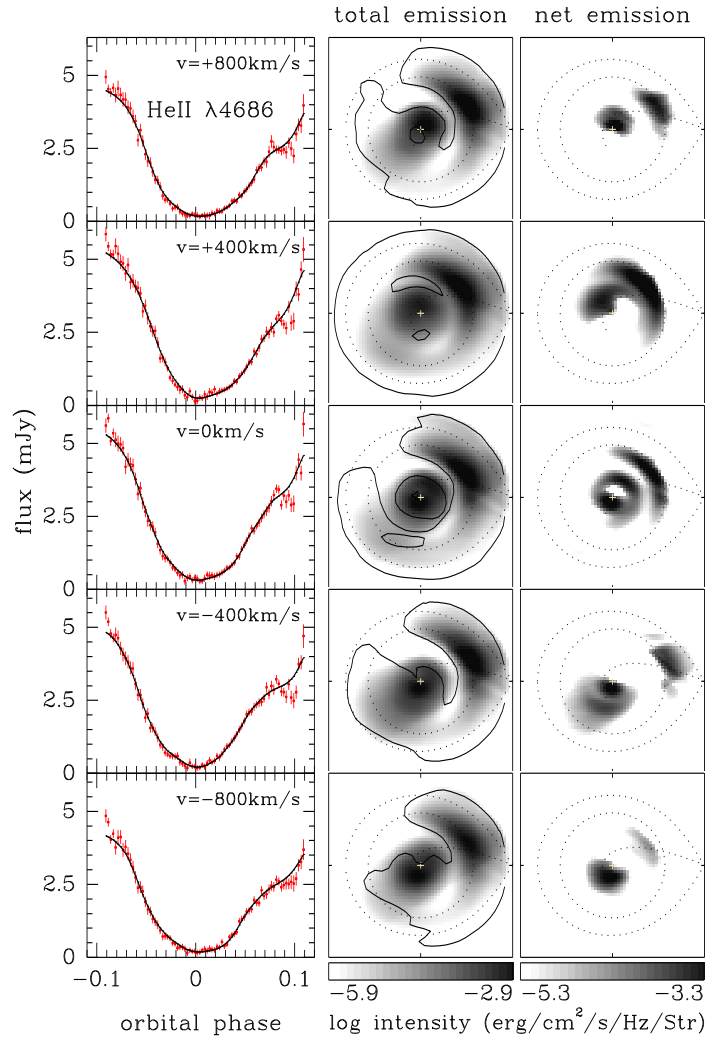


Fig. 3.— Velocity-resolved light curves (left) and eclipse maps (middle and right) for He II 4686. The notation is similar to that of Fig. 2.

trajectory with the disk rim. This azimuthally-extended bright spot indicates that the shock of the inflowing gas with the outer disk is radiatively inefficient, with the emission pattern spreading along the direction of gas rotation. Moreover, if the bright spot cannot cool efficiently it should also expand in the vertical direction, leading to a vertically-extended bulge in the outer disk that becomes a natural site for reprocessing of x-ray radiation from the rotating magnetic poles – in line with the findings of Saito & Baptista (2009). From the radial position of the maximum intensity of the bright spot, we estimate an outer disk radius of $R_{BS} = 0.57 \pm 0.03 R_{L1}$.

In order to emphasize the structures observed in the line maps, we calculated net line emission maps. These were obtained by combining continuum eclipse maps on the short and long wavelength sides of the target emission line and by subtracting the derived average continuum map from each of the velocity resolved line maps. Because of our choice to display the maps in a logarithmic grayscale (that only handles positive intensities), regions where the resulting intensities are negative (indicating line absorption) were suppressed from the net line emission maps shown in Figs. 2 and 3. The Balmer lines net emission maps show a dearth of emission at the bright spot position, indicating that these lines are in absorption at the infalling stream impact site (see Section 4.2). In contrast, the He II 4686 line appears clearly in emission at the bright spot position (Fig. 3, right-hand panels). The emission is stronger in the positive velocity maps but weak blueshifted emission is also seen in the -400 and -800 km s^{-1} velocity maps. The latter is likely the result of gas splashing away from the accretion disk (with a velocity component towards the observer) after the collision of the infalling gas stream with the disk rim. The redshifted emission reflects the fact that disk gas at the bright spot position is mostly moving towards the far side of the disk and, therefore, away from the observer.

Because the temperatures in the outer disk regions ($T \simeq 6000 - 7000 \text{ K}$, see Section 4.5)

are not enough to power the high-excitation He II 4686 line, the strong He II emission from this region is an indication that the bright spot must be an important source of reprocessing of x-ray radiation from the magnetic poles/curtains – again in line with the findings of Saito & Baptista (2009). This is consistent with and leads to a natural explanation for the results of Patterson et al. (1978) — who found that the amplitude of the 71 s pulsations is variable along the orbit and reaches maximum around phase $\phi \sim 0.25$ — and of O’Donoghue (1985) — who correctly advanced the conclusion that the orbital behavior of the 71 s pulsations amplitude requires that the x-ray reprocessing site be a disk rim with variable thickness and maximum visibility at phases 0.2 – 0.3. This coincides with the phase range where the upper side of the azimuthally- and vertically-extended bright spot is best seen.

The zero-velocity H β net line emission map shows a peculiar “heart”-shaped distribution close to disk center ($R < 0.3 R_{L1}$) with major axis aligned at an angle of $\simeq 150^\circ$ with respect to the line joining both stars (Fig. 2). Morphologically similar structures are also seen in the ± 200 and $\pm 400 \text{ km s}^{-1}$ velocity maps, with the positive velocity maps showing the receding part of the structure (i.e., the upper hemisphere of the eclipse maps in Figs. 2 and 3) and the negative velocity maps showing the leading part of the structure (i.e., the lower hemisphere of the eclipse maps in Figs. 2 and 3). An asymmetric structure resembling a dipole pattern and aligned at a similar orientation can be seen in the zero-velocity He II 4686 net emission map (Fig. 3). We will return to this point in Section 5.2.

4.2. Spatially resolved spectra

Motivated by the distinct emission observed at the bright spot and gas stream regions and in order to avoid contamination by bright spot emission that could affect the spectrum of the near side of the disk (the hemisphere closest to the secondary star in the eclipse

maps of Figs. 2 and 3), we divided the eclipse maps in two distinct regions: “disk” and “gas stream”. We define the “disk” as the disk section between azimuths 90° and 270° , and “gas stream” as the region between azimuths 0° and 90° (see Fig. 4). We further defined annular sections of width $0.1 R_{L1}$ to extract spatially-resolved spectra as a function of radius. In order to isolate the contribution of possible asymmetric brightness sources in the eclipse maps (e.g., the bright spot, gas stream or accretion curtains) we separated the total emission into its symmetric and asymmetric disk emission components. The symmetric component is obtained by slicing the disk into a set of radial bins, computing the average of the lower half of the intensities in each bin, and fitting a smooth spline function to the resulting set. The spline fitted intensity in each annular section is taken as the symmetric component. The asymmetric component is obtained by subtracting the symmetric component from the original eclipse map. This procedure essentially preserves the baseline of the radial profile, removing all azimuthal structure from the symmetric component. The statistical uncertainties affecting the fitted intensities are estimated with a Monte Carlo procedure (Section 3.2).

Fig. 5 shows spatially resolved spectra for the symmetric disk component and for the “gas stream” region (total emission). In the inner regions ($R \lesssim 0.2 R_{L1}$) the disk spectrum shows a flat and featureless continuum with no Balmer or HeII lines. The disk spectrum becomes progressively redder and fainter with increasing radius, indicating the existence of a radial temperature gradient. The Balmer and HeII lines start to appear in emission at intermediate disk regions ($R \simeq 0.3 R_{L1}$) and become stronger with increasing radii. The spectrum of the “gas stream” is systematically bluer and brighter than the disk spectrum at the same radius and the difference increases with radius. In contrast to the observer in the disk spectra, in the outer regions ($R > 0.5 R_{L1}$) the lines appear in absorption, indicating that the emitting gas is optically thick. The P Cygni profile of the Balmer lines in the “gas stream” spectrum framing the bright spot, at $R = (0.5 - 0.6) R_{L1}$, is an indication that

part of the colliding gas stream deflects back towards the observer, in agreement with the inference previously drawn from the He II $\lambda 4686$ net emission line maps.

The lack of Balmer lines in the innermost disk regions may be interpreted in a scenario of magnetically-controlled accretion for radii smaller than the Alfvén radius. Assuming for DQ Her a white dwarf mass of $M_1 = 0.6 M_\odot$ (Zhang et al. 1995), an accretion rate of $\dot{M} = 2.7 \times 10^{-9} M_\odot \text{ yr}^{-1}$ (Section 4.5) and a white dwarf magnetic moment in the range $\mu = 10^{32} - 10^{33} \text{ G cm}^3$ (typical for intermediate polars, Patterson 1994), we estimate an Alfvén radius for DQ Her in the range $R_A \simeq (0.05 - 0.25) R_{L1}$. It is expected that inside this radius the disk will be disrupted, with the gas being channelled by the magnetic field lines onto accretion curtains down to the magnetic poles at the white dwarf surface. This produces magneto-*bremstrahlung* (free-free) radiation by the optically thin gas, which leads to a spectrum basically flat for the spectral range between the self-absorption limit and a thermal-cutoff. Hence, the spectrum observed in the innermost disk regions (i.e., flat and featureless) could plausibly be interpreted in this context (Kraft 1959; Wickramasinghe 1988).

A relatively narrow (FWHM $\lesssim 400 \text{ km s}^{-1}$) and redshifted (by $\simeq 200 \text{ km s}^{-1}$) Ca II $\lambda 3934$ absorption line can be seen both in the disk and in the gas stream spectra up to $R \sim 0.3 R_{L1}$. (There are hints that a similarly narrow and redshifted Ca II $\lambda 3968$ absorption line is also present in the disk and gas stream spectra at the same radial range, although we assign a low weight to this statement as this line is heavily blended with the broad $H\epsilon$ emission line.) This corresponds to the Ca II s-wave seen in absorption in the trailed spectrogram of the same data set and which Martell et al. (1995) associated to the accretion disk.

Could the Ca II line be the result of absorption of disk radiation by a cool and vertically-extended disk rim along the line of sight? The evidences say no. If this was the

case, the line strength would increase with radius for spectra of the near side of the disk since the obscuration effect increases as one moves towards the disk rim in the near side. On the contrary, the observed CaII line strength decreases with increasing radius in the spectra of the “gas stream” (Fig. 5) as well as in the symmetric component of spectra extracted for the near side of the disk (not shown here).

The temperatures inferred for the inner disk regions ($T > 10^4 K$, see Section 4.5) are too high to allow for significant CaII emission. Thus, the CaII absorption should be produced in intervening cooler gas along the line of sight. Interesting inferences can be drawn from the dynamics of this intervening gas. Gas rotating in Keplerian orbits at this distance from the white dwarf should lead to broad (FWHM $\sim 1000 - 3000 \text{ km s}^{-1}$) and double-peaked absorption lines with no blueshift/redshift. The observed narrow, single-peaked and redshifted CaII line indicates that the gas dynamics in the absorbing region is dominated by radial motion (in opposition to azimuthal, Keplerian motion). Depending on where the absorption occurs along the line of sight, we may be witnessing gas outflow (if absorption occurs closer to the orbital plane, at the far side of the disk) or gas inflow (if absorption occurs closer to the observer along the line of sight, at the near side of the disk).

In the radial outflow scenario DQ Her would be acting as a propeller (e.g., Wynn et al. 1997), expelling gas from inside the magnetosphere towards larger radii. The corotation radius for DQ Her ($R_{co} = 0.031 R_{\odot} = 0.041 R_{L1}$) is comparable to (and even smaller than) our lower estimate of the Alfvén radius, suggesting that plasma blobs that attach to field lines at $R_{co} < R < R_A$ should be centrifugally accelerated (Warner 1995, Chapter 7). Accordingly, one would expect to see blueshifted CaII absorption in spectra of the near side of the disk in account of gas expelled towards the observer. However, contrary to this expectation, the CaII absorption line is also redshifted both in the “gas stream”

spectra and in the symmetric component of spectra extracted for the near side of the disk. Additional problems with this scenario include the difficulties to explain why the outflow velocity would be so low ($v_{out} \simeq 200 \text{ km s}^{-1}$), why it does not change with radius, and why no Ca II absorption is seen in the outer disk regions.

The radial inflow alternative leads to a magnetically-controlled accretion scenario, in which the Ca II absorption line is produced when relatively cool regions of the accretion curtain are seen projected against hot gas in the background. Inside the magnetosphere ($R < R_A$) two effects contribute to broaden the emission/absorption lines: (i) the gas corotates with the white dwarf magnetic field, the spin velocity of which increases with radius, $v_\phi = R\omega_{\text{spin}}$; (ii) at the same time, gas moves inwards along field lines with a radial velocity $v_r \leq v_{ff} \propto R^{-1/2}$. Because DQ Her is a fast rotator, large azimuthal velocities ($v_\phi \simeq 2300 - 12000 \text{ km s}^{-1}$) are expected for the range of radii of interest, $R = 0.05 - 0.25 R_{L1}$, and lines produced in this region should be quite broad. Then, why is the Ca II line so narrow?

At this point it is worth noting that because an eclipse map yields a snapshot of the eclipsed brightness distribution over a time scale much longer than the 71 s pulsation period, the contribution of the rapidly rotating magnetosphere to our spatially-resolved spectra is a time averaged spectrum over all orientations (or, pulse phases). Adopting the oblique dipole accretor model of (Saito & Baptista 2009, see their Fig. 3), significant absorption should occur around spin phase $\phi_{\text{spin}} = 0.5$ — when the upper accretion curtain covers the largest portion of the hot inner magnetosphere and/or the (also hot) innermost regions of the far side of the accretion disk. However, at this orientation the spin component of the accretion curtain velocity field is mostly in the plane of the sky and the projected velocity along the line of sight is essentially v_r . Note that, at quadrature ($\phi_{\text{spin}} = 0.25$ and 0.75), the absorption of radiation by the upper accretion curtain is not only significantly reduced

but is also smeared in wavelength because of the contribution of a large spin velocity component to the line profile. Thus, the observed absorption line profile is dominated by the spectral contribution of the accretion curtains at $\phi_{\text{spin}} = 0.5$. The magnetically-controlled accretion scenario implies radial inflow velocities of $v_r \sim 200 \text{ km s}^{-1}$, significantly lower than both the rotational and the free-fall velocities for that range of radii. This is line with inferences drawn by Wu & Wickramasinghe (1991), who pointed out that, for rapidly rotating intermediate polars, the accretion shock may occur almost at R_A and the infall from R_A to the white dwarf surface is unlikely to have a significant radial component.

4.3. The emission lines

In this section we analyse the radial behavior of Balmer ($\text{H}\beta$, $\text{H}\gamma$ and $\text{H}\delta$) as well as the HeII 4686 lines. Fig. 6 shows the radial intensity distribution for the lines and for the adjacent continuum (top), the radial intensity distribution for the net line emission (second row from top), the radial run of the equivalent width (EW, third row from top) and the radial run of the full width at half-maximum (FWHM, bottom). The diagrams were derived from the symmetric disk component (Section 4.2). The performance of the eclipse mapping technique to reconstruct FWHM distributions is discussed in the Appendix A.

The intensities in the line maps are higher than in the adjacent continuum at intermediate and outer disk regions, indicating that the lines appear in emission there. The Balmer lines disappear in the continuum in the innermost disk regions ($R < 0.2 R_{L1}$), and the corresponding net line emission becomes unreliable or meaningless. For $\text{H}\gamma$ and $\text{H}\delta$ the line intensity is lower than the continuum level at disk center indicating that these lines are in absorption there. These regions are not plotted in the corresponding net emission panels.

The net line emission decreases in strength with increasing radius in the intermediate

and outer disk regions. The radial dependence has a particular slope for each line, indicating that the empirical law $I \propto r^{-1.5}$ (Marsh et al. 1990) is not adequate to describe the behavior of the emission lines in DQ Her. Moreover, we found that, for the Balmer lines, the radial dependence is linearly correlated with the energy required to excite the line. This result will be discussed in Section 5.1.

The EW of the Balmer lines increase with radius with maxima of $EW \simeq 100 - 400 \text{ \AA}$ at $R = 0.5 R_{L1}$. In contrast, the HeII 4686 line shows an $EW \simeq 20 \text{ \AA}$, roughly independent of radius. In all cases, the EW becomes negligible (or negative) at the innermost disk regions because the continuum intensities reach (or exceed) the line intensities.

In the intermediate and outer disk regions ($R \geq 0.3 R_{L1}$) the slope of the observed FWHM distribution of the Balmer lines is fairly consistent with the expected $v_K \propto R^{-1/2}$ law for gas rotating in Keplerian orbits. However, the observed FWHM values are systematically lower than the predicted for a disk around a white dwarf with $M_1 = 0.6 M_\odot$ (the dashed line in the lowermost panels of Fig. 6) by $\sim 30\text{-}40\%$, suggesting that either the adopted white dwarf mass is overestimated or that the emitting gas has sub-Keplerian velocities. No reasonable error in the estimated inclination could account for this discrepancy. Moreover, in order to reconcile the Keplerian velocity distribution with the observed FWHM values, an unrealistically low-mass white dwarf ($\leq 0.35 M_\odot$) would be needed. It is therefore likely that the disk gas has sub-Keplerian velocities. The HeII 4686 FWHM is hard to measure and becomes unreliable for $R \gtrsim 0.3 R_{L1}$, because the net line intensity is decreasing sharply with radius and the EW is relatively small.

Fig. 7 shows the velocity profile for the total and the asymmetric component of the emission lines. In the total emission spectra the lines appear in emission in the intermediate and outer regions ($R \gtrsim 0.2 R_{L1}$) becoming progressively sharper (stronger and narrower) with increasing radius. The Balmer and the HeII 4686 lines show a clear double-peaked

profile with the blue peak generally stronger than the red peak in the Balmer lines. The He II line changes from a double-peaked profile at small radii to a single-peaked profile in the outer disk regions.

The differences in behavior between the Balmer lines and the He II 4686 line has already been observed in previous analyses of DQ Her. The 71 s pulsation, evident in He II, is absent (Chanan et al. 1978) or negligible (Martell et al. 1995) in the Balmer lines. This result reflects the different ionization/excitation conditions between hydrogen and heavier ions.

The spectra of the asymmetric component evince inverse P-Cygni profiles for all lines, with a 'red' absorption component on top of a 'blue' emission peak. The strength of the absorption component decreases with increasing radius and disappears for $R > 0.4 R_{L1}$. The $H\beta$ absorption component is narrow and slightly blueshifted (by $\simeq -200 \text{ km s}^{-1}$) in the innermost regions, and progressively broadens and moves towards positive velocities with increasing radius, reaching trough velocities of $\simeq +500 \text{ km s}^{-1}$ at $R = (0.3 - 0.4) R_{L1}$. The absorption component is always redshifted for the other lines, also with velocities of $\simeq +500 \text{ km s}^{-1}$. The emission components are centered at $\simeq -500 \text{ km s}^{-1}$. The blueshifted emission seen in spectra of the asymmetric component of the far side of the disk indicates that emitting gas of a non axi-symmetric brightness source is falling radially towards the white dwarf at disk center. Consistently, absorbing gas along the line of sight (possibly at the near side of the disk) is also falling radially towards the white dwarf at disk center with similar radial inflow velocities ($v_r \sim 500 \text{ km s}^{-1}$). These evidences are in agreement with those inferred from the behavior of the Ca II $\lambda 3934$ absorption line; they give additional support to the magnetically-controlled accretion scenario put forward in the preceding section.

4.4. The uneclipsed component

At the high inclination of DQ Her, there is no region in the far side of the disk which is never eclipsed and, therefore, it is not possible to dump extra flux at mid-eclipse without affecting the shape of the model eclipse light curve. Any extra flux at mid-eclipse is unambiguously attributed to 'uneclipsed light', i.e., the fraction of the total light which cannot be included in the eclipse map. Thus, the uneclipsed component in DQ Her arises from light outside of its orbital plane (or from the outward-facing hemisphere of the eclipsing secondary star).

Fig. 8 shows the uneclipsed component and its fractional contribution with respect to the average out-of-eclipse level. The uneclipsed spectrum is dominated by the Balmer lines, which appear in emission with an apparent double-peaked profile. $H\beta$ is the most prominent line, reaching $\simeq 25\%$ of the total emission at its wavelength. The He I $\lambda 4921$ line is also strong in the spectrum, at a level similar to that of $H\delta$ but with a wider line profile. In contrast to the observed in the average spectra (in- and out-of-eclipse), where the continuum is almost flat, the continuum in the uneclipsed component rises towards longer wavelengths, reaching the same intensity level of some lines (e.g., the He ϵ line). A close inspection indicate that the uneclipsed Balmer lines have a shallow and narrow central absorption core (FWHM $\simeq 200 \text{ km s}^{-1}$) on top of a broader emission component (FWHM $\simeq 800 \text{ km s}^{-1}$). The absorption core of the He I $\lambda 4921$ line is deeper and wider, with a FWHM $\simeq 600 \text{ km s}^{-1}$.

It is unlikely that the uneclipsed emission lines are from the secondary star. Although trailed spectra of Balmer lines show an emission component with the secondary star motion, the emission comes from the inward-facing hemisphere of the secondary star — indicating it is caused by irradiation effects — and is apparently restricted to orbital phases around $\phi \sim 0.5$ — suggesting that the emitting region is not visible during eclipse (Martell et al.

1995). As the inward-facing hemisphere of the secondary star is not seen around eclipse, it should not contribute to the uneclipsed light. Furthermore, the width of the uneclipsed lines is much larger than expected for a rotationally broadened line from the secondary star in DQ Her ($V_{\text{rot}} \sin i = 115 \pm 18 \text{ km s}^{-1}$, Horne et al. 1993).

The uneclipsed emission lines are probably from the nova shell. We note that nebular emission from the extended nova shell was included in the slit together with the light from the binary, and its contribution was not removed from the spectra (Martell et al. 1995). Accordingly, the FWHM of the uneclipsed emission lines is consistent with the expansion velocity of the nova shell ($v = 370 \pm 14 \text{ km s}^{-1}$, see Vaytet et al. 2007). The narrow absorption component possibly arises in a collimated and optically thick wind from the accretion disk. Evidences for the presence of a collimated disk wind in DQ Her come from the eclipse behavior of the CIV $\lambda 1550$ resonance line (Eracleous et al. 1998), the study of scattered x-ray emission (Mukai et al. 2003), and from the ellipsoidal shape of the nova shell and the ablation of gas clumps around the shell poles (Vaytet et al. 2007). The secondary star may be responsible for the rising continuum at the red end of the spectrum, although the short wavelength range where the continuum appears prevents a meaningful attempt to infer its spectral type.

4.5. The temperatures of the disk

Here we fit isothermal, pure hydrogen atmosphere models (HI), to the spatially resolved spectra at each disk annular region (Fig. 5) in order to derive the radial dependence of temperature and column density in the disk (Fig. 9). We used the symmetric component of the emission and we masked the regions of the lines, since the models only account for the continuum emission produced by bound-free and free-free HI transitions. The fit depends on the solid angle θ^2 assumed for the pixel in the eclipse maps, which by its turn depends

on the distance and the inclination with which the pixel is seen by an observer at the Earth. The effective inclination of a pixel in the far side of the accretion disk is $i_{eff} = i - \beta$, where β is the disk half-opening angle. We obtained fits for distances of 400 pc (Horne et al. 1993) and 525 pc (Vaytet et al. 2007), and half-opening angles of $\beta = 0^\circ$, 2° , and 3.5° .

Fig. 9 shows the resulting radial dependence of the temperature and column density for the case $d = 400 pc$ and $\beta = 2^\circ$ (solid line with filled triangles) and $d = 525 pc$ and $\beta = 2^\circ$ (open circles). Also shown are the results for two extreme cases of low (larger distance and lower β) and high (lower distance and larger β) θ^2 . The χ^2 of the fit increases perceptibly for $d = 525 pc$, because the high temperatures required to match the average flux level of the spectra can no longer reproduce the red slope of the observed spectra. Although the different choices of θ^2 lead to systematic differences in temperature and column density, these differences are of the order of the uncertainties affecting the derived quantities and do not alter the inferences that can be drawn from Fig. 9. Our results (for $d = 400 pc$ and $\alpha = 2^\circ$) indicate that the surface density increases with increasing radius, showing values of $\Sigma \sim 4 \times 10^{-5} g cm^{-2}$ at $R = 0.15 R_{L1}$ and $\Sigma \sim 3 \times 10^2 g cm^{-2}$ at $R = 0.65 R_{L1}$. The steady-state disk models predict that the surface density is proportional to $\alpha^{-4/5} R^{-3/4}$, where α is the viscosity parameter. Thus, our values for Σ are consistent with steady-state model only if the viscosity in the disk decreases with increasing radius in order to compensate the factor $\propto R^{-3/4}$. The brightness temperature ranges between $T \simeq 13500 K$ at $R = 0.15 R_{L1}$ and $T \simeq 5000 K$ at $R = 0.65 R_{L1}$, with a radial dependence reasonably well described by a steady-state optically thick disk model with mass accretion rate of $\dot{M} = (2.7 \pm 1.0) \times 10^{-9} M_\odot yr^{-1}$. The inferred mass accretion rate is in reasonable agreement with the values derived by (Chanan et al. 1978, $\dot{M} = 10^{-9} M_\odot yr^{-1}$) and (Zhang et al. 1995, $\dot{M} = 3.4 \times 10^{-9} M_\odot yr^{-1}$).

Temperatures in excess of 8000 K are required in order to produce the strong lines

with shallow Balmer decrement observed in the intermediate and outer disk regions. This is in contrast with the low temperatures ($T \lesssim 5500 K$) inferred from the slope of the red continuum emission, suggesting the existence of a vertical temperature gradient in the DQ Her disk gas, with a hot, optically thin chromospheric layer (responsible for the emission lines) on top a cool, opaque and dense disk photosphere (responsible for the red continuum). The chromosphere is likely heated by irradiation of x-ray photons from the magnetic poles and accretion curtains, leading to high-excitation lines. This scenario is beyond LTE simple models.

Smak (1981) remarks that in DQ Her the continuum emission seems to be a function of the accretion disk regime while the line emission appears to be correlated with the luminosity or surface temperature of the primary star. In this context the lines are formed by reprocessing of the energy radiated from the central source, probably the accreting material falling over the magnetic poles of the white dwarf. This central emission in DQ Her can be detected in soft x-ray emission (Mukai et al. 2003).

We note that the temperatures in the outer disk regions ($R \gtrsim 0.3 R_{L1}$) are systematically below the critical temperature for disk instabilities to set in (Warner 1995), suggesting that the DQ Her disk could show dwarf nova-type outbursts. This holds even if one assumes the higher mass accretion rate of Zhang et al. (1995) (illustrated by the steady-state disk model with $\dot{M} = 10^{-8.5}$ in Fig. 9). There is no record of dwarf nova outbursts in this binary.

We end this section raising a puzzlingly different scenario from the radial temperature distribution of Fig. 9. Given the evidences presented here of magnetically-controlled accretion for $R \lesssim 0.3 R_{L1}$, it is reasonable to assume that a *bona fide* accretion disk exists only for distances outside this range, and that the brake in slope of the temperature and column density distributions at $R \sim 0.3 R_{L1}$ reflects the change from the azimuthal flow of gas in the outer accretion disk to a magnetically-controlled radial flow of gas over the

accretion curtains in the inner regions. In this case, the outer accretion disk shows a flat temperature distribution resembling those found in quiescent dwarf novae (e.g., Wood et al. 1986, 1992). The inferred low temperatures ($T \sim 6000 K$) and high surface densities ($\Sigma \sim 10^4 g cm^{-2}$) suggest that the disk viscosity is low. This is in marked contrast to the common view that the old nova DQ Her is a nova-like variable with a hot, viscous accretion disk.

5. Discussion

5.1. An energy dependency of the emission-line radial intensity distribution slope

In Section 4.3 we found that the slope of the radial line intensity distributions correlates with the transition energy of the Balmer lines. In order to extend our analysis we extracted (using the same procedures described in Section 4.3) the radial intensity distribution for H ϵ , the next line in the Balmer series. We then fitted a power-law $I \propto r^{-\alpha}$ (e.g., Smak 1981; Horne & Marsh 1986) for each radial distribution in order to find the best-fit α index for each line. The innermost disk regions ($R < 0.2 R_{L1}$) are excluded from the fit since the continuum reaches the emission level of the lines in the regions inside this radius. The results are listed in Table 1 and plotted in Fig. 10.

The α index increases with the transition energy for the Balmer lines, i.e., the emission at lines with larger transition energy (e.g., H ϵ) are more concentrated at the disk center than lines of lower energy (e.g., H β). Moreover, our results reveal that there is a strong linear correlation between α and the transition energy for the Balmer lines (see Fig. 10). This result is in contrast with the empirical $I \propto r^{-1.5}$ law (Marsh et al. 1990) usually evoked in works about radial distribution of emission lines in accretion disks. The He II 4686 line

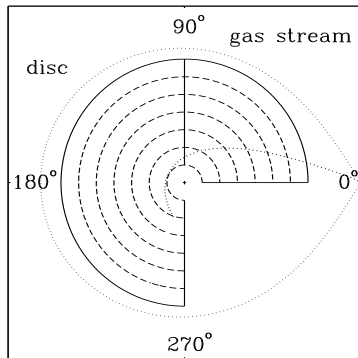


Fig. 4.— Schematic diagram showing the regions defined as “disc” and “gas stream”. Dashed lines mark the annular regions of width $0.1 R_{L1}$ used to extract spatially resolved spectra. Dotted lines show the projection of the primary Roche lobe onto the orbital plane and the gas stream trajectory. Azimuths are measured with respect to the line joining both stars and increase counter-clockwise. Four reference azimuths are labeled in the figure.

Table 1: Index α for the Balmer series and He II lines.

Line	E[eV]	α ($I \propto r^{-\alpha}$)
H β	12.76	1.20 ± 0.06
H γ	13.06	2.16 ± 0.11
H δ	13.23	2.62 ± 0.10
H ϵ	13.33	2.95 ± 0.12
He II 4686	75.50	3.15 ± 0.14

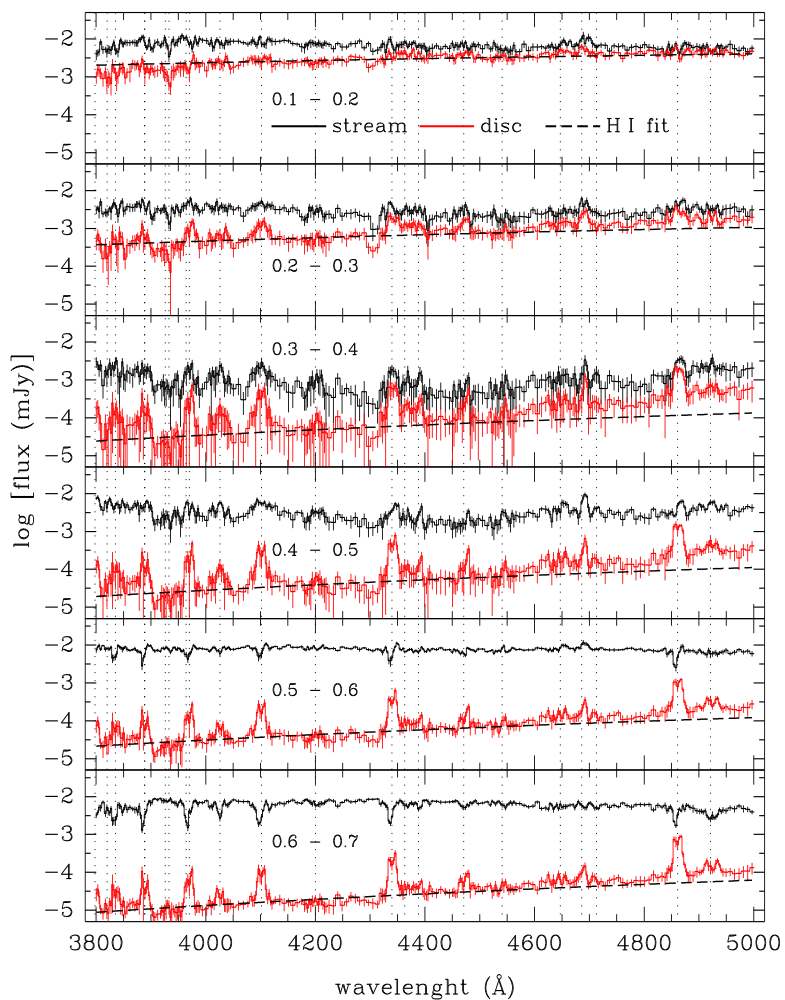


Fig. 5.— Spatially resolved spectra for the sections defined as “disk” ($90^\circ - 270^\circ$, light grey) and “gas stream” ($0^\circ - 90^\circ$, dark grey) for a set of six annular regions (labels in units of R_{L1}). Dashed lines show the best-fit H I model for the disk spectra. Vertical dotted lines mark the major transition lines of the spectra.

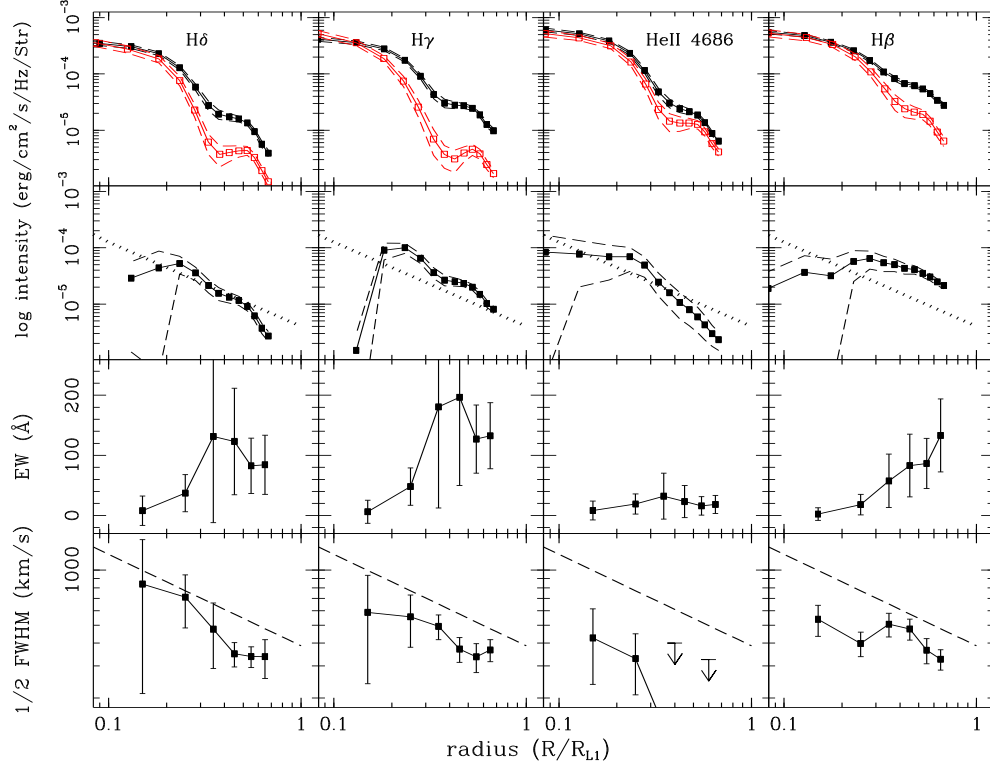


Fig. 6.— Top: Radial intensity distributions of selected optical lines (filled symbols) and of the corresponding adjacent continuum (open symbols). Dashed lines indicate the 1σ limit in each case. Second row from the top: Net line emission radial distributions. Dotted lines show the $I \propto r^{-1.5}$ radial dependence, derived by Marsh et al. (1990). Third from top: EW as a function of radius. Bottom: FWHM of the lines as a function of radius. Dashed lines show the law $v \propto r^{-1/2}$ expected for gas rotating in Keplerian orbits around a white dwarf of mass $M_1 = 0.6 M_\odot$. The predicted spin velocity of material channelled by the white dwarf magnetic field is too high to appear in the velocity range plotted in the panels (see text).

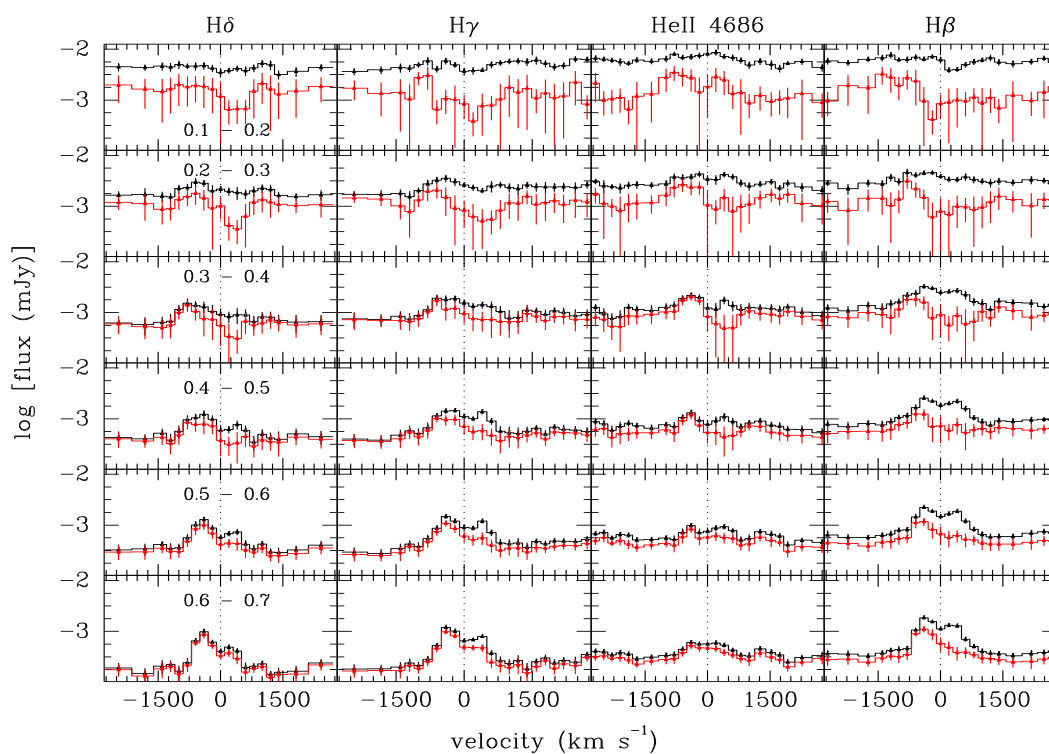


Fig. 7.— The velocity resolved spectra for the four most prominent emission lines in the DQ Her spectra comparing the total emission (black) and the asymmetric component emission (grey). Vertical dotted lines mark the line center in each case

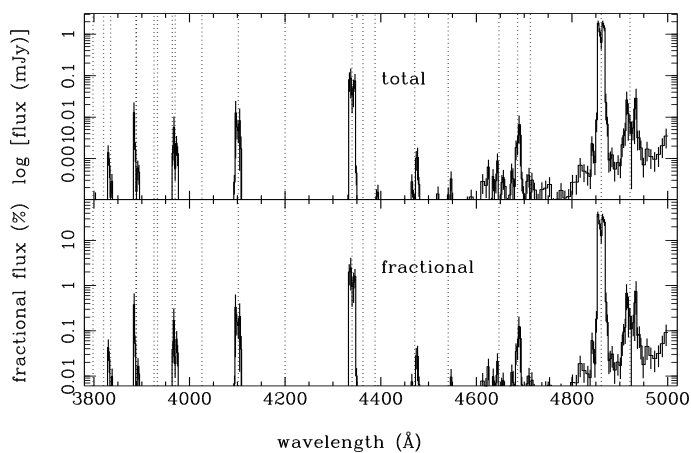


Fig. 8.— Spectrum of the uneclipsed component. Top: total contribution. Bottom: fractional contribution. The notation is similar to that of Fig. 5.

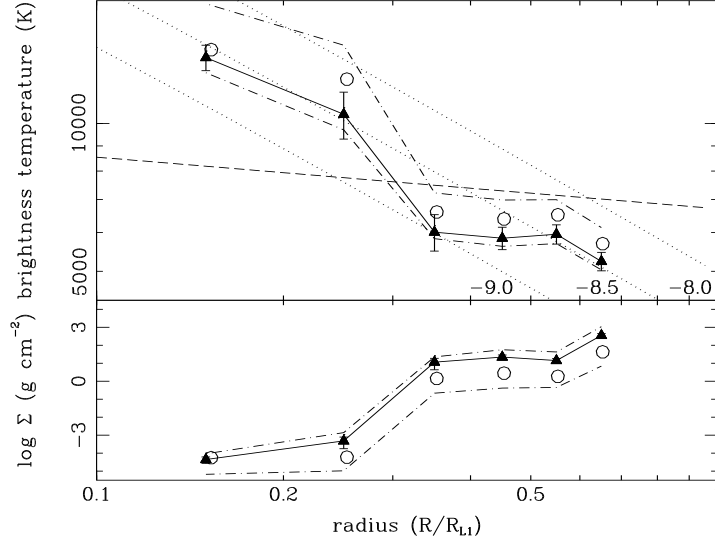


Fig. 9.— Top: The radial run of the brightness temperature of the best-fit HI model to the disk spectra ($d = 400 pc$ and $\beta = 2^\circ$, solid line with filled triangles) and for $d = 525 pc$ and $\beta = 2^\circ$ (open circles). The results for two alternative, extreme cases of low ($d = 525 pc$ and $\beta = 0^\circ$) and high ($d = 400 pc$ and $\beta = 3.5^\circ$) solid angles (see text) are shown as the upper and lower dot-dashed curves, respectively. Dotted lines show steady-state disk models for mass accretion rates of $\dot{M} = 10^{-8.0}$, $10^{-8.5}$ and $10^{-9.0} M_\odot \text{ yr}^{-1}$. The dashed line shows the critical temperature above which the gas should remain in a steady, high- \dot{M} regime, according to the disk instability model. Bottom: the radial run of the surface density. The notation is the same as for the upper panel.

radial distribution falls much more rapidly with radius than the Balmer lines, with an $\alpha = 3.15$, and does not fit the linear relation of the Balmer lines. This is not surprising, as significantly different physical conditions are required to produce the H I and He II lines.

Smak (1969) and Huang (1972) showed that the double-peaked profile of emission lines in accretion disks can be accounted for by making two basic assumptions: (i) the geometry is flat, i.e., the disk emission is restricted to the orbital plane, and (ii) the disk is in Keplerian motion. Smak (1981) showed that the line profile is sensitive to the line radial intensity distribution and that the α value could be recovered by fitting a model to the line profile. From observational evidences (e.g., Fabian et al. 1979; Young & Schneider 1980) he found that the emission lines profiles could be represented by power-laws $I \propto r^{-\alpha}$, where α is expected to be in the range 1 – 2.

Smak (1981) gives a list of results where α could be estimated for Helium and Balmer series lines (Z Cha, Fabian et al. 1979; SS Cyg, Cowley et al. 1980; Stover et al. 1980; HT Cas, Young et al. 1981; DQ Her, Hutchings et al. 1979; Dmitrienko & Cherepashchuk 1980). In all cases the value obtained for α is in the range 1.7 – 2.2 suggesting that there are no systematic differences between objects of different classes of cataclysmic variables. Similar values of α are obtained by fitting the line profile of the dwarf novae U Gem or Z Cha and the intermediate polar DQ Her. Hutchings et al. (1979) found that in DQ Her the H β line has $\alpha = 2.2$ while He II 4686 has $\alpha = 1.9$. These values are inconsistent with our results. The discrepancy may be explained by the low spectral resolution of the data of Hutchings et al. (1979), which obtained α from line profiles of low resolution (dispersion of 48 \AA mm^{-1}) while we extracted α from spatially resolved spectra obtained from data of significantly higher spectral resolution (2 \AA pixel^{-1}).

Marsh (1987) analysed the Balmer lines in the dwarf nova Z Cha. In his study the differences between the line profiles in the average spectrum are evident. The line wings

become wider from $H\alpha$ to $H\delta$ indicating that the radial line distributions become more concentrated for increasing transition energy. In quiescence, Z Cha has a relatively small inferred mass transfer rate of $\dot{M} = 10^{-12} M_{\odot} yr^{-1}$. Simulations shows that the LTE model is not valid in this case, producing a poor fit to the Balmer lines (Marsh 1987).

Marsh (1988) found $\alpha = 1.8$ for the Balmer lines in the dwarf nova IP Peg in quiescence. Similarly, Marsh & Horne (1990) showed that in IP Peg the radial distribution of the Balmer lines have similar slopes when the object is in quiescence but that the radial distributions are different for distinct lines when the object is in outburst. The $H\delta$ line distribution is steeper than $H\gamma$, that is steeper than $H\beta$, i.e., the α index of the radial profile increases with the transition energy. A similar result was found by Marsh et al. (1990) for the dwarf nova U Gem, with $H\gamma$ and $H\beta$ showing, respectively, $\alpha = 1.66$ e 1.43 . In contrast, for the white dwarf V2051 Oph, Saito & Baptista (2006) found $\alpha = 1.55$ for $H\delta$ and $\alpha = 1.78$ for $H\gamma$; α decreases with the transition energy in this dwarf nova. During their observations V2051 Oph was in an unusual low brightness state (low mass transfer rate). Thus, there are observational evidences that the slope of the radial line distribution is different for different emission lines.

In order to understand the physics behind the line formation in accretion disks it is necessary to combine new and improved theory with spatially-resolved observational studies. Spatially resolved studies from Doppler tomography and eclipse mapping techniques can provide high resolution information about the line distribution in the accretion disk. More sophisticated spectral models for accretion disk need to include features such as the vertical temperature structure and external sources of heat.

5.2. Are we seeing the accretion curtains?

Here we discuss possible interpretations for the asymmetries seen in the low-velocity eclipse maps of the $H\beta$ and He II $\lambda 4686$ lines. These asymmetries cannot be explained in terms of gas stream overflow (e.g., Baptista & Bortoletto 2004, see their Fig. 5) as they are physically unrelated to the gas stream trajectory, nor can they be interpreted in terms of spiral shock waves (e.g., Baptista et al. 2000, see their Fig. 2) as the morphology, orientation and location are inconsistent with those expected for two-armed tidally-induced spiral structures. Moreover, it is also not possible to explain the observed structures in terms of a front-back asymmetry caused by a flared disk (e.g., Baptista et al. 1998, see their Figs. 3 and 8) because this would affect both line and continuum maps, whereas in DQ Her the asymmetries are only seen at specific velocity-resolved eclipse maps of particular emission lines. Additionally, the disk opening angle is not large enough to result in measurable obscuration or limb-darkening effects (see Section 3.2). The asymmetries observed in the $H\beta$ and He II $\lambda 4686$ line maps seem to be of a different nature, related to something not previously seen in eclipse mapping experiments.

DQ Her is the first intermediate polar being eclipse mapped. It is tempting to interpret the structures seen in the low-velocity He II and $H\beta$ maps in terms of the projection onto the orbital plane of accretion columns/curtains formed over the magnetic poles of the white dwarf by the channeled material (e.g., Ferrario 1996)². In this scenario, due to

²The eclipse mapping procedure has the approximate effect of projecting any emission from above the orbital plane back along the inclined line of sight to the point where it pierces the disk plane. Thus, emission arising at height Z above the disk is projected a distance $Z \tan i$ towards the back of the disk and is distorted by the intrinsic azimuthal smearing effect of the eclipse mapping method (Baptista et al. 1995). With our choice of azimuthal blur width $\Delta\phi$ (Section 3.2), any point source in the eclipse maps will appear smeared in

different opacities for incoming irradiating photons, and energies needed to ionize atoms and to excite electrons to the upper energy levels of each transition, the regions of the accretion curtains close to the magnetic poles are prone to reprocess the strong irradiation by hard x-rays photons whereas regions farther away receive less energetic photons. Hence, high-excitation lines such as He II $\lambda 4686$ trace the emission in the accretion curtains regions closer to the magnetic poles, whereas the low-excitation Balmer lines trace emission from regions farther away from the x-ray emitting magnetic poles. Lines of different excitation frame different parts of the accretion flow and, individually, yield only a partial view of the emitting accretion curtains. According to this, a better view of the accretion curtains may be obtained by combining the complementary high-excitation He II map with the low-excitation $H\beta$ map. An eclipse map obtained by combining the net line emission He II $\lambda 4686$ and $H\beta$ low-velocity eclipse maps is shown in Fig. 11. A remarkable structure resembling a twisted dipole emitting pattern can be seen near disk center. Although this figure encourages one to further pursue this line of reasoning, it poses an immediate problem.

Each eclipse map yields a snapshot of the disk brightness distribution averaged over the period covered by the 4 eclipses. Therefore, because it comprises a timescale much longer than the 71 s spin period of the white dwarf, changes in brightness distribution caused by the varying aspect of the accretion curtains with the white dwarf rotation should be completely smeared out in the eclipse map — just as in a long exposure picture of a moving target. How could one then obtain a coherent image of fast rotating accretion curtains in an eclipse map? The answer can be built in terms of the selection in velocity for the accreting material performed by the application of spectral mapping techniques.

The velocity field for gas in the accretion curtains is a sum of its inflowing component

azimuth by $\simeq 20^\circ$.

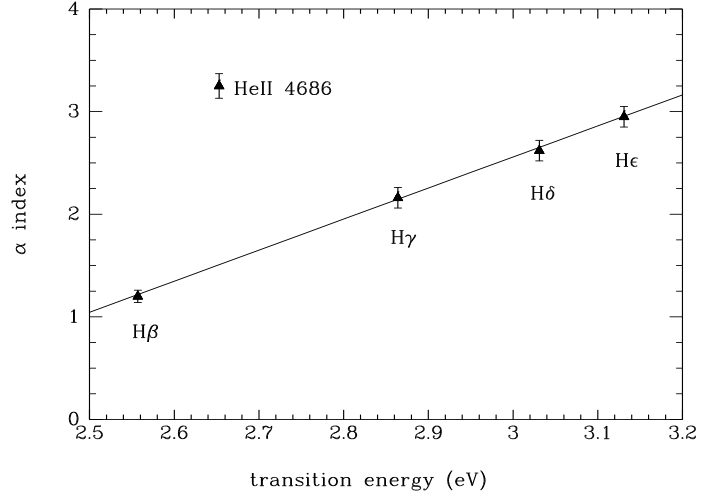


Fig. 10.— Distribution of the index α in function of the transition energy for the HeII 4686 and Balmer series lines. The solid line marks a linear fit for the Balmer lines distribution (see Section 5.1).

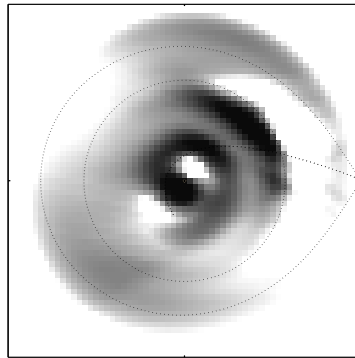


Fig. 11.— Combined net emission HeII plus $H\beta$ low-velocity eclipse map. The notation is similar to that of Fig. 2.

(along the magnetic field lines) and a rotational component (due to the white dwarf spin period). As seen in Sections 4.2 and 4.3, the velocity field is dominated by the rotational component, which is significantly larger than the inflowing component. At most rotation phases (i.e., curtain orientations), different parts of the curtains show distinct projected velocities along the line of sight and their emission will split onto several different velocity bins across the emission line profile. Conversely, a specific velocity-resolved eclipse map will contain a mixture of different parts of the accretion curtains at different rotation phases. This slicing and mixing effect prevents one from obtaining a coherent image of the accretion curtains at all velocity-resolved eclipse maps, with the fortunate exception of the low-velocity bin.

When the curtains are aligned with the binary axis — and only at this orientation — the rotational component will be suppressed (because it becomes orthogonal to the line of sight), and the curtains will show only the small inflowing velocity component (see Section 4.2), contributing to the same particular low-velocity bin. We note that two effects contribute to further reduce the observed projected velocity: (i) the inflow velocity must decrease after the accretion shock until it reaches zero at the white dwarf surface, and (ii) for accretion curtains twisted off the orbital plane, regions close to the magnetic poles present the lowest projected velocity along the line of sight. Therefore, looking at a low velocity bin is equivalent of framing the accretion curtains always at the same two spin phases (where the curtains are oriented at an azimuth roughly aligned with the binary main axis), allowing one to obtain a coherent image of them.

A further question is why the accretion curtains lag the binary main axis by $\simeq 30^\circ$. Hellier (1999) applied Doppler tomography techniques to spin-pulse spectroscopy of intermediate polars to find that the optical pulsation arises from azimuthally-extended accretion curtains, located typically a few white dwarf radii from disk center. His tomogram

of the slow rotator PQ Gem shows a twist in the accretion curtains, with material feeding onto magnetic field lines $\sim 40^\circ$ ahead of the location at which it hits the white dwarf. This is the opposite case of what is seen in DQ Her and the difference may be in the spin period. For comparable magnetic field strengths and mass accretion rates a slow rotator (the case of PQ Gem, $P_{spin} = 834\text{ s}$) picks material at a magnetospheric radius with higher (Keplerian) velocity than the accretion curtains. Thus, the accretion curtains tend to step ahead of the magnetic pole. On the other hand, in a fast rotator (the case of DQ Her, $P_{spin} = 71\text{ s}$) the field lines at the magnetosphere are rotating faster than the disk gas being channelled onto the field lines (see Section 4.3). In this case the accretion curtains tends to lag the magnetic pole.

6. Summary

We applied eclipse mapping techniques to spectroscopy covering 4 eclipses of DQ Her in order to isolate the emission from different parts of its accretion flow as well as from outside the orbital plane. The main results of this study can be summarized as follows:

1. Velocity-resolved eclipse maps of the $H\beta$ and He II $\lambda 4686$ lines indicate the presence of an azimuthally- and vertically-extended bright spot at disk rim (at $R_{BS} = 0.57 \pm 0.03 R_{L1}$), which is an important source of reprocessing of x-rays from the magnetic poles. This is in line with the conclusion that the bright spot is the main site of the 71 s optical pulsations in DQ Her (Saito & Baptista 2009).
2. In the inner regions the disk spectrum is flat with no Balmer or Helium lines, suggesting that the emission arises from *bremsstrahlung* radiation by an optically thin gas. In the intermediate and outer disk regions the spectrum shows double-peaked emission lines typical of a rotating disk gas. The slope of the continuum becomes

progressively redder with increasing radius, indicating the existence of a radial temperature gradient.

3. We fit LTE HI emission models to the flux and slope of the continuum in order to infer the temperature and the surface density of the emitting gas. The surface density increases by six orders of magnitude from the inner to the outer disk regions. The temperatures are in the range $T \simeq 13500 - 5000 \text{ K}$ (for $R = [0.15 - 0.65] R_{L1}$) and can be reasonably well described by a steady-state disk with a mass accretion rate of $\dot{M} = (2.7 \pm 1.0) \times 10^{-9} M_{\odot} \text{ yr}^{-1}$. The strong emission lines with shallow Balmer decrement observed in the outer disk regions are in contrast to the low temperatures inferred from the slope of the continuum, suggesting an outer disk structure with a hot and optically thin chromosphere (responsible for the emission lines) on top of a cool, opaque and dense disk photosphere (responsible for the continuum emission).
4. The narrow and redshifted Ca II $\lambda 3934$ absorption line in the total light spectra and the inverse P-Cygni profiles of the Balmer and He II $\lambda 4686$ emission lines in spectra of the asymmetric component of the eclipse maps indicate radial inflow of gas in the inner disk regions ($R < 0.3 R_{L1}$), and are best explained in terms of magnetically-controlled accretion inwards of the white dwarf magnetosphere in DQ Her. We infer projected radial inflow velocities of $(200 - 500) \text{ km s}^{-1}$, significantly lower than both the rotational and the free-fall velocities for the corresponding range of radii.
5. The combined net emission He II plus H β low-velocity eclipse map shows a twisted dipole emitting pattern near disk center. This is interpreted as being the projection of accretion curtains onto the orbital plane at two specific spin phases, as a consequence of the selection in velocity provided by the spectral eclipse mapping. This is in line with and strengthen the above inference.

6. The spectrum of the uneclipsed light is dominated by Balmer and HeI lines in emission with narrow absorption cores. The line emission is probably from the extended nova shell, whereas the narrow absorption likely arises in a collimated and optically thick wind from the accretion disk.
7. A comparison of the line radial distribution for the Balmer lines reveals a linear correlation between the slope of the distribution and the transition energy.

The white dwarf atmosphere models used in the work were kindly provided by Dr. Detlev Koester. We thank João Steiner for an enlightening discussion which led to the novel application of eclipse mapping techniques to map the 71 s optical pulsations in DQ Her (Saito & Baptista 2009). This work was partially supported by CNPq/Brazil through the research grant 62.0053/01-1– PADCT III/Milenio. RS acknowledges financial support from CONICYT through GEMINI Project Nr. 32080016, BASAL PFB-06, FONDAP Center for Astrophysics Nr. 15010003 and CNPq/Brazil. RB acknowledges financial support from CNPq/Brazil through grants n. 300.354/96-7 and 301.442/2004-5.

A. Reconstruction of FWHM distributions of emission lines

Here we address the reliability of spectral mapping techniques to reconstruct FWHM distributions of emission lines from spatially resolved disk spectra. Our aim is to check whether the sub-Keplerian velocities found for the Balmer and HeII 4686 lines in DQ Her (Section 4.3) are intrinsic to the variable or an artifact of the mapping method.

First, we created a synthetic eclipse map of a steady-state opaque accretion disk according to the set of parameters of DQ Her: white dwarf mass of $M_1 = 0.6 M_\odot$ (Zhang et al. 1995), white dwarf radius of $R_{WD} = 0.0121 R_\odot$ (Martell et al. 1995), Roche

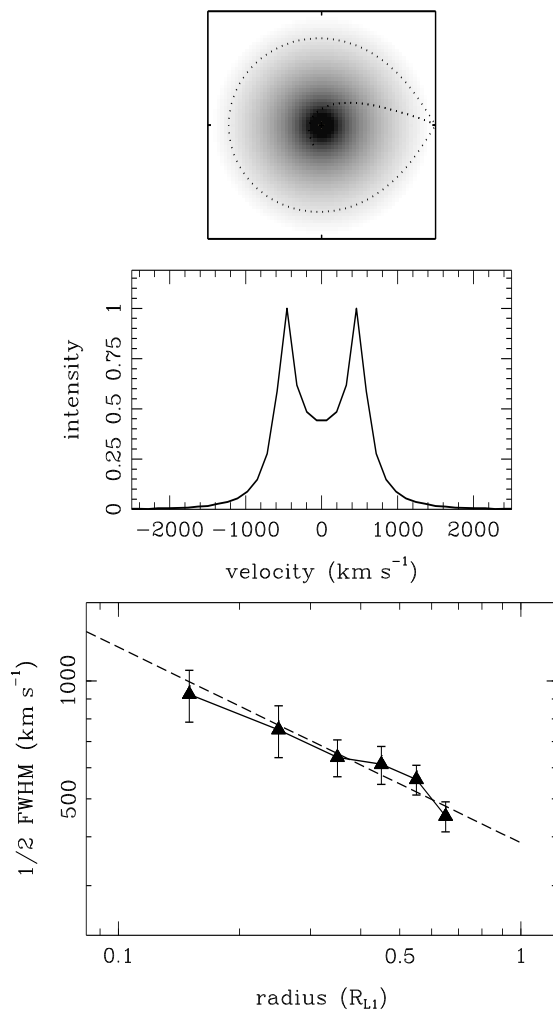


Fig. 12.— Top: Greyscale plot of the brightness distribution of the steady-state disk used in the simulation. Middle: the emission line profile derived from the brightness distribution of the top panel assuming a Keplerian velocity field according to the parameters of DQ Her. Bottom: The FWHM of the emission line as a function of radius derived from the spectral mapping of 23 light curves along the emission line profile of the middle panel. A dotted line shows the $v \propto r^{-1/2}$ law expected for Keplerian orbits around a white dwarf of mass $M_1 = 0.6 M_\odot$.

lobe size of $R_{L1} = 0.766 R_{\odot}$ (Petterson 1980) and an accretion rate of $\dot{M} = 2.7 \times 10^{-9} M_{\odot} \text{ yr}^{-1}$ (Section 4.5). We adopted the geometry of DQ Her ($i = 86.5^{\circ}$ and $q = 0.66$, Horne et al. 1993) to simulate the eclipse of this brightness distribution and to generate velocity-resolved synthetic light curves for the same set of bins used in the spectral mapping of DQ Her (Section 3.1). In order to construct the light curve of a given velocity bin, we assumed a Keplerian velocity field for the synthetic eclipse map and computed, at each orbital phase, the flux contribution only for those pixels the projected (Doppler) velocity of which falls inside the velocity bin under consideration. The intensity distribution of the synthetic map is shown in the upper panel and the corresponding double-peaked emission line profile is depicted in the middle panel of Fig. 12.

Gaussian noise was added to the synthetic light curves to simulate the signal-to-noise ratio of the DQ Her data and eclipse mapping techniques were applied to the resulting light curves to generate a set of velocity-resolved synthetic eclipse maps (see Section 3.2). We combined the velocity-resolved maps to derive spatially-resolved spectra for the same set of radial annuli used in the analysis of the DQ Her data, and we extracted the FWHM distribution of the emission line as a function of radius following the same procedure used in Section 4.3. The lower panel of Fig. 12 compares the derived FWHM distribution with the $v \propto r^{-1/2}$ law used to construct the original eclipse map. Uncertainties were derived via Monte Carlo simulations with the synthetic light curves.

The derived FWHM distribution is in good agreement with the Keplerian expectation (at the $1-\sigma$ confidence level) at all radii. These simulations show that the FWHM distribution of emission lines can be reliably recovered from spatially-resolved spectra of accretion disks obtained with eclipse mapping techniques. This exercise indicates that the sub-Keplerian velocity distributions observed in the DQ Her lines are intrinsic to the variable and not an artifact of the mapping procedure.

REFERENCES

- Africano, J. L., & Olson, E. C. 1981, *PASP*, 93, 130
- Baptista, R. 2001, *Astrotomography, Indirect Imaging Methods in Observational Astronomy*, 573, 307
- Baptista, R., & Catalán, M. S. 2001, *MNRAS*, 324, 599
- Baptista, R., Harlaftis, E. T., & Steeghs, D. 2000, *MNRAS*, 314, 727
- Baptista, R., Horne, K., Hilditch, R. W., Mason, K. O., & Drew, J. E. 1995, *ApJ*, 448, 395
- Baptista, R., Horne, K., Wade, R. A., Hubeny, I., Long, K. S., & Rutten, R. G. M. 1998, *MNRAS*, 298, 1079
- Baptista, R., & Steiner, J. E. 1993, *A&A*, 277, 331
- Baptista, R., Steiner, J. E., & Horne, K. 1996, *MNRAS*, 282, 99
- Baptista, R., & Bortoletto, A. 2004, *AJ*, 128, 411
- Chanan, G. A., Nelson, J. E., & Margon, B. 1978, *ApJ*, 226, 963
- Cowley, A. P., Crampton, D., & Hutchings, J. B. 1980, *ApJ*, 241, 269
- Dmitrienko, E. S., & Cherepashchuk, A. M. 1980, *AZh*, 57, 749
- Eracleous, M., Livio, M., Williams, R. E., Horne, K., Patterson, J., Martell, P., & Korista, K. T. 1998, *Wild Stars in the Old West*, 137, 438
- Fabian, A. C., Pringle, J. E., Whelan, J. A. J., & Bailey, J. A. 1979, *IAU Colloq. 46: Changing Trends in Variable Star Research*, 65
- Ferrario, L. 1996, *Publications of the Astronomical Society of Australia*, 13, 87

- Hellier, C. 1999, *ApJ*, 519, 324
- Hellier, C. 2001, *Cataclysmic Variable Stars*, Springer, 2001,
- Horne, K. 1985, *MNRAS*, 213, 129
- Horne, K., & Marsh, T. R. 1986, *MNRAS*, 218, 761
- Horne, K., Welsh, W. F., & Wade, R. A. 1993, *ApJ*, 410, 357
- Huang, S.-S. 1972, *ApJ*, 171, 549
- Hutchings, J. B., Cowley, A. P., & Crampton, D. 1979, *ApJ*, 232, 500
- Kraft, R. P. 1959, *ApJ*, 130, 110
- Marsh, T. R. 1987, *MNRAS*, 228, 779
- Marsh, T. R. 1988, *MNRAS*, 231, 1117
- Marsh, T. R., & Horne, K. 1988, *MNRAS*, 235, 269
- Marsh, T. R., & Horne, K. 1990, *ApJ*, 349, 593
- Marsh, T. R., Horne, K., Schlegel, E. M., Honeycutt, R. K., & Kaitchuck, R. H. 1990, *ApJ*, 364, 637
- Martell, P. J., Horne, K., Price, C. M., & Gomer, R. H. 1995, *ApJ*, 448, 380
- Mukai, K., Still, M., & Ringwald, F. A. 2003, *ApJ*, 594, 428
- O'Donoghue, D., 1985, in *Proc. Ninth American Workshop on Cataclysmic Variables*, ed. P. Szkody (Seattle: Univ. Washington), p. 98
- Patterson, J. 1994, *PASP*, 106, 209

- Patterson, J., Robinson, E. L., & Nather, R. E. 1978, *ApJ*, 224, 570
- Petterson, J. A. 1980, *ApJ*, 241, 247
- Rutten, R. G. M., Kuulkers, E., Vogt, N., & van Paradijs, J. 1992, *A&A*, 265, 159
- Saito, R. K., & Baptista, R. 2006, *AJ*, 131, 2185
- Saito, R. K., & Baptista, R. 2009, *ApJ*, 693, L16
- Smak, J. 1969, *Acta Astronomica*, 19, 155
- Smak, J. 1981, *Acta Astronomica*, 31, 395
- Stover, R. J., Robinson, E. L., Nather, R. E., & Montemayor, T. J. 1980, *ApJ*, 240, 597
- Vaytet, N. M. H., O’Brien, T. J., & Rushton, A. P. 2007, *MNRAS*, 380, 175
- Walker, M. F. 1956, *ApJ*, 123, 68
- Warner, B. 1986, *Ap&SS*, 118, 271
- Warner, B. 1995, *Cambridge Astrophysics Series*, Cambridge, New York: Cambridge University Press, —c1995,
- Wickramasinghe, D. T. 1988, *Polarized Radiation of Circumstellar Origin*, 199
- Wood, J., Horne, K., Berriman, G., Wade, R., O’Donoghue, D., & Warner, B. 1986, *MNRAS*, 219, 629
- Wood, J. H., Horne, K., & Vennes, S. 1992, *ApJ*, 385, 294
- Wu, K., & Wickramasinghe, D. T. 1991, *MNRAS*, 252, 386
- Wynn, G. A., King, A. R., & Horne, K. 1997, *MNRAS*, 286, 436

Young, P., & Schneider, D. P. 1980, ApJ, 238, 955

Young, P., Schneider, D. P., & Shectman, S. A. 1981, ApJ, 245, 1035

Zhang, E., Robinson, E. L., Stiening, R. F., & Horne, K. 1995, ApJ, 454, 447